Supplementary Information

Neodymium isotopes as a paleo-water mass tracer: A model-data reassessment

Frerk Pöppelmeier[a,b,*], Jörg Lippold[c], Patrick Blaser[d], Marcus Gutjahr[e], Martin Frank[e], Thomas F. Stocker[a,b]

[a]Climate and Environmental Physics, Physics Institute, University of Bern, Bern, Switzerland

[b]Oeschger Centre for Climate Change Research, University of Bern, Bern, Switzerland

[c]Institute of Earth Sciences, Heidelberg University, Heidelberg, Germany

[d]Institute of Earth Sciences, University of Lausanne, Lausanne, Switzerland

[e]GEOMAR Helmholtz Centre for Ocean Research Kiel, Kiel, Germany

***Corresponding author:** Frerk Pöppelmeier (frerk.poeppelmeier@unibe.ch)

Text S1: Model tuning for the pre-industrial state.

A number of new parameterizations have been implemented here for the first time (see section 2.1), which required a re-tuning of the Nd module. Overall, this was done analogous to Pöppelmeier et al. (2020), with only some minor differences that are described here. The parameters that were varied are the magnitude of the benthic Nd flux, the riverine Nd scaling, and the scavenging efficiency. In contrast to Pöppelmeier et al. (2020), we here considered particle-dependent scavenging efficiencies (as K_D coefficients) for each of the four particle types (POM, $CaCO_3$, biogenic opal, and dust). Since we therefore were required to tune a greater number of parameters, we performed a Latin hypercube sampling of that six-dimensional parameter space. As such, we were also able to explore a larger range of the parameter space without the need for an exceedingly large number of simulations. In total, our tuning ensemble consisted of 450 members. To determine the simulation that best agrees with the updated seawater dataset (see main text), we calculated the Mean Absolute Error (MAE) for both, the dissolved Nd concentration and εNd (including all water depth, compared to the exclusion of the top 250 m in Pöppelmeier et al., 2020). The corresponding tuning parameters for the best fit simulation are listed in Table S1. The changes in the Nd source apportionment compared to Pöppelmeier et al. (2020) are fairly small with the dust flux now contributing 8%, the riverine flux 39%, and the benthic flux 53% to the total Nd input compared to previously 9%, 32%, and 60%, respectively. In absolute terms, the dust flux is now 0.5×10^9 g/yr, the riverine flux is 2.5×10^9 g/yr, and the benthic flux is 3.4×10^9 g/yr.

Text S2: Binary mixing calculation of %NSW.

For the εNd-based calculation of the Atlantic-wide NSW fraction we assumed simple binary water mass mixing. We defined the end-members as the zonal average Nd concentrations and εNd signatures at 60°S – 3.1 km and 50°N – 2.6 km, since they cannot be defined at the surface due to local inputs. Yet, we note that these calculations are not particularly sensitive to the exact locations of the end-members. Following this, we calculated the NSW fraction at each grid cell *x* from the zonally averaged Nd concentration and isotope signature based on:

$$\%NSW(x)=\frac{[Nd]_S(\varepsilon_X-\varepsilon_S)}{\varepsilon_X([Nd]_S-[Nd]_N)+\varepsilon_N[Nd]_N-\varepsilon_S[Nd]_S} \quad (1)$$

where subscripts N and S refer to the northern, and southern end-member, respectively, and ε is the εNd signature.

To derive only the conservative part of the Atlantic-wide εNd distribution, we make use of the true water mass distribution as simulated by the dye tracer. For this, we re-normalize the latter by the Nd end-member characteristics as follows:

$$\varepsilon_{dye}=\frac{\%NSW_{dye}(\varepsilon_N[Nd]_N-\varepsilon_S[Nd]_S)+\varepsilon_S[Nd]_S}{\%NSW_{dye}([Nd]_N-[Nd]_S)+[Nd]_S} \quad (2)$$

with $\%NSW_{dye}$ being the fraction of NSW based on the dye tracer. The non-conservative part is than the difference between the simulated εNd distribution and ε_{dye} as depicted in Figure 3.

Table S1: Re-tuned parameters of the Nd module. All other parameters remained unchanged compared to Pöppelmeier et al. (2020).

Parameter	Old value (Pöppelmeier et al., 2020)	New value
Benthic flux (g/yr)	3.3×10^9	3.4×10^9
River redissolution factor	3.5	3.4
POM scavenging coefficient	$C_p/C_d = 0.0014$	3.5×10^5
$CaCO_3$ scavenging coefficient	$C_p/C_d = 0.0014$	3.0×10^5
Biogenic opal scavenging coefficient	$C_p/C_d = 0.0014$	8.0×10^5
Dust scavenging coefficient	$C_p/C_d = 0.0014$	3.0×10^5
Particle sinking velocity (m/yr)	1000	1000 (but scaled with vertical density gradient)
Residence time (yr)	690	715
MAE ([Nd], n = 2485) (pmol/kg)	5.22 (re-evaluated)	5.04
MAE (εNd, n = 2647)	1.34 (re-evaluated)	1.23

Table S2: Model forcings for the LGM and transient simulations, respectively.

LGM

Parameter	Value	Reference	Transient scaling
Orbital	20 kyr BP	Berger (1978)	Berger (1978)
CO_2	191 ppm	Köhler et al. (2017)	Köhler et al. (2017)
CH_4	370 ppb	Köhler et al. (2017)	Köhler et al. (2017)
N_2O	208 ppb	Köhler et al. (2017)	Köhler et al. (2017)
Ice sheets	LGM extent	Peltier (1994)	Lisiecki and Stern (2016)
Wind stress	PMIP3 anomalies	Pöppelmeier et al. (2021)	Benthic $\delta^{18}O$
Diapycnal diffusivity	Wilmes et al. (2019)	Pöppelmeier et al. (2021)	Benthic $\delta^{18}O$
ToA aerosol forcing	–2.5 W/m^2 (relative to PI)	Hopcroft et al. (2015)	Benthic $\delta^{18}O$
POM remineralization	Figure S4	This study	Benthic $\delta^{18}O$
Dust field	LGM	Mahowald et al. (2006)	Benthic $\delta^{18}O$
Riverine Nd flux	–10% (relative to PI)	This study	Benthic $\delta^{18}O$
N. Atl. riverine Nd flux	–90% (relative to PI)	This study	Benthic $\delta^{18}O$
Iceland riverine Nd flux	+500% (relative to PI)	This study	Benthic $\delta^{18}O$
N. Atlantic benthic flux	Background level	This study; Pöppelmeier et al. (2020)	Benthic $\delta^{18}O$
Additional transient forcing			
N. Atlantic freshwater	Figure S11	Menviel et al. (2012)	
Bering strait opening	At 12 kyr BP	Pico et al. (2020)	
Additional N. Atlantic benthic Nd flux	10.5–8 kyr BP	Pöppelmeier et al. (2020)	

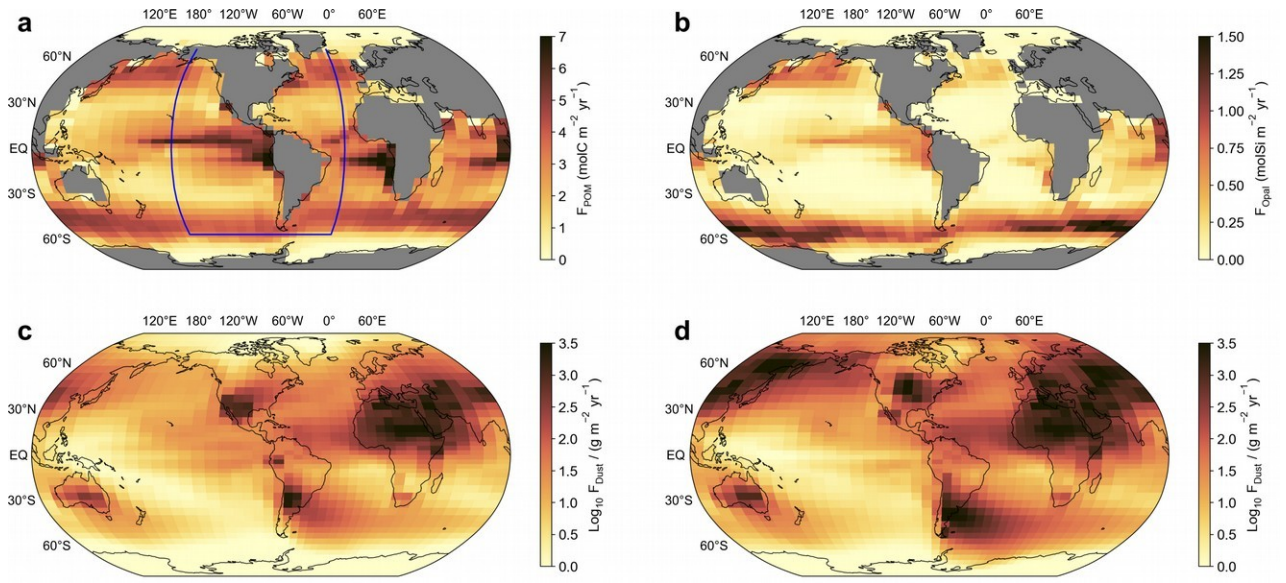

Figure S1: (a) Export flux of particulate organic matter (POM), and **(b)** biogenic opal for the pre-industrial control simulation. Blue line in panel a marks the global transect used for Figures 1, 5, and 8. **(c)** Dust flux as prescribed for the pre-industrial and **(d)** the Last Glacial maximum on a Log10 color scale both after Mahowald et al. (2006).

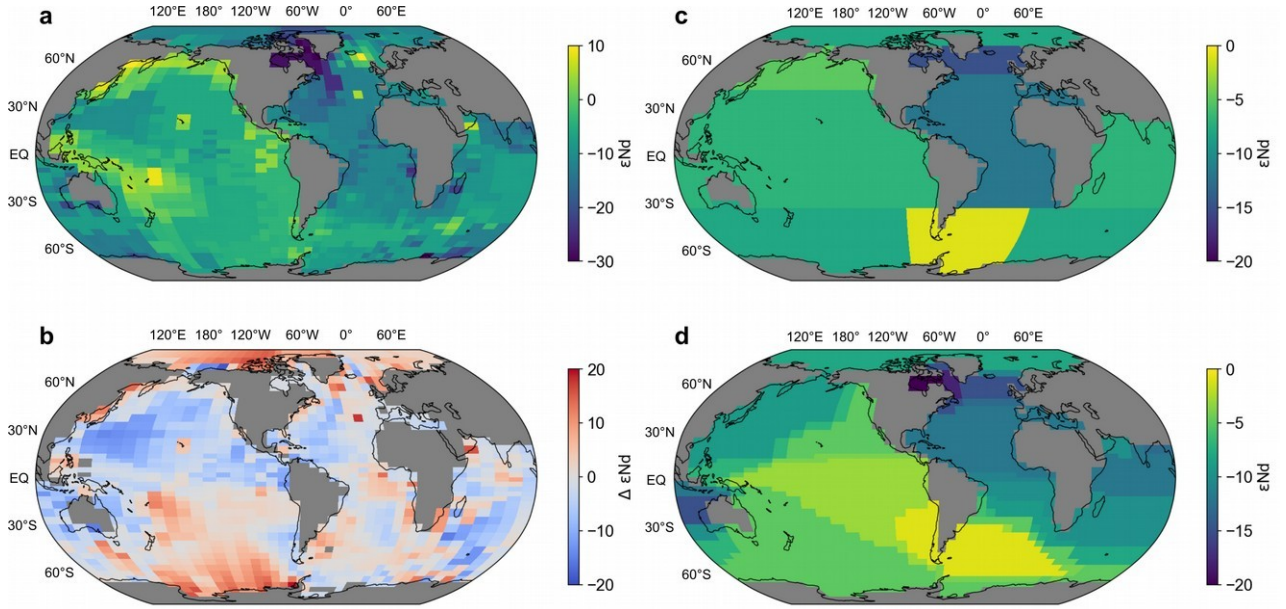

Figure S2: (a) New detrital εNd map by Robinson et al. (2021) regridded on the Bern3D grid, and **(b)** difference to the previously used map by Pöppelmeier et al. (2020). **(c)** Nd isotopic signatures of the dust source as first described by Tachikawa et al. (2003). **(d)** Updated εNd map of the dust source based on the dust plume expansion by Mahowald et al. (2006) and the mean isotopic signatures of the dust sources.

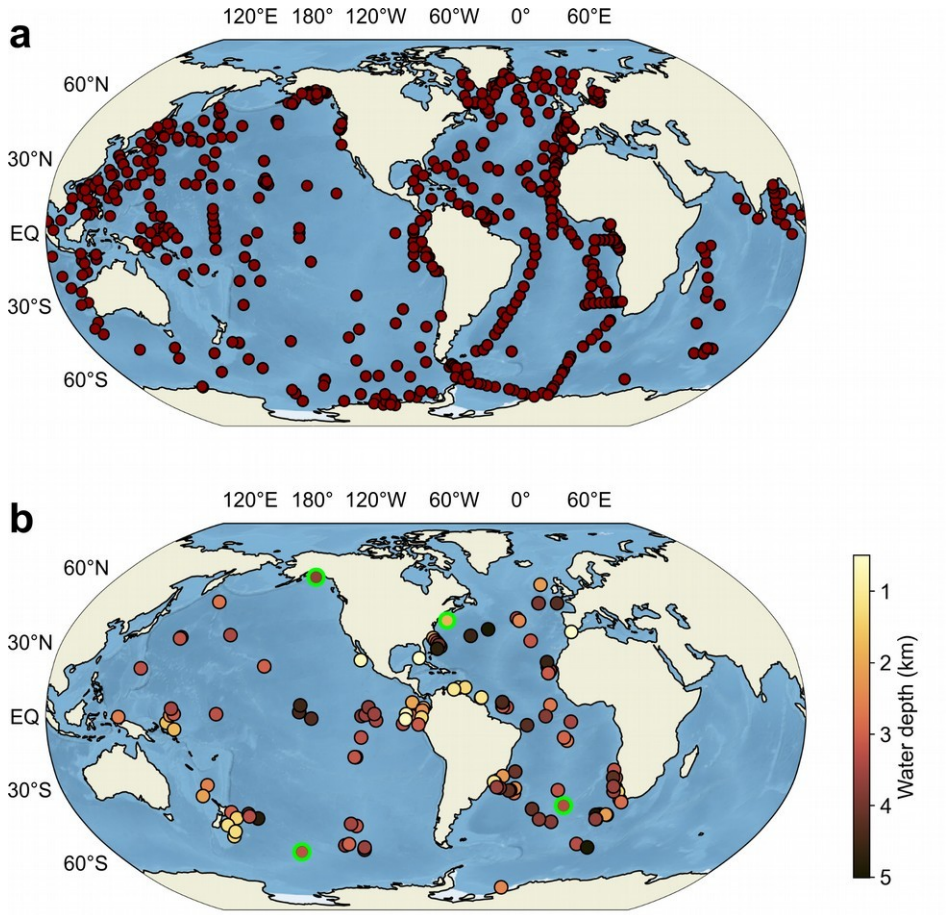

Figure S3: (a) Global maps depicting all seawater stations and **(b)** sediment cores used for the evaluation of the pre-industrial and LGM, respectively. Circles with green edges in panel b mark εNd records to which the transient simulations are compared to. Compilation of the Nd isotope data of the LGM are listed in supplementary Table S3.

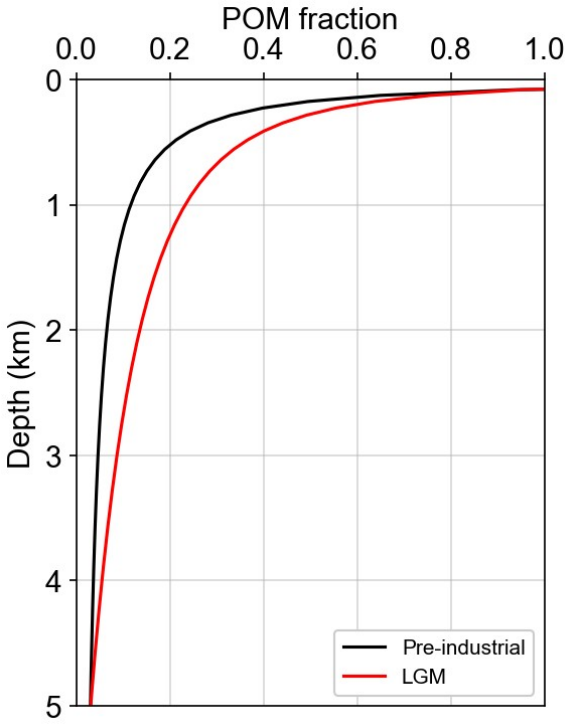

Figure S4: Particulate organic matter (POM) remineralization profiles for the pre-industrial control after Martin et al. (1987) (black) and as adjusted for the LGM (red). For the transient evolution the remineralization profile was linearly scaled between these two curves based on the benthic $\delta^{18}O$ stack of Lisiecki and Stern (2016).

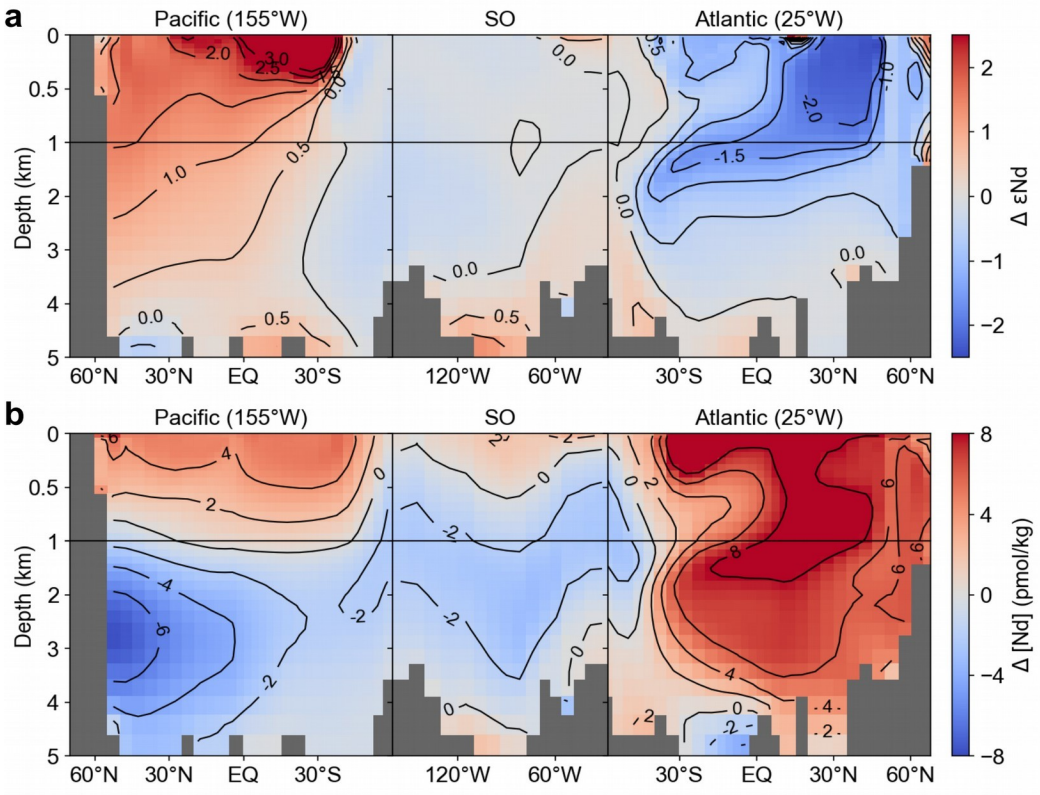

Figure S5: Difference of **(a)** εNd and **(b)** the Nd concentration of the new pre-industrial control and the previous implementation by Pöppelmeier et al. (2020).

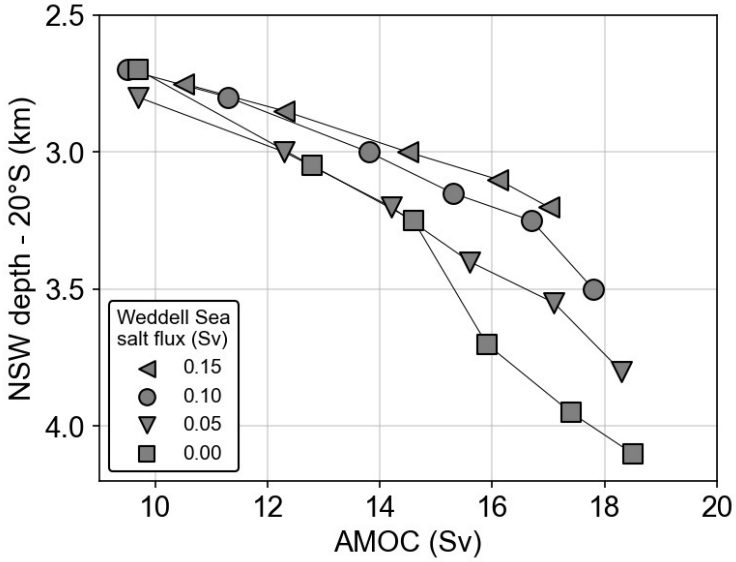

Figure S6: NSW depth – AMOC strength parameter space covered by the 24 LGM simulations.

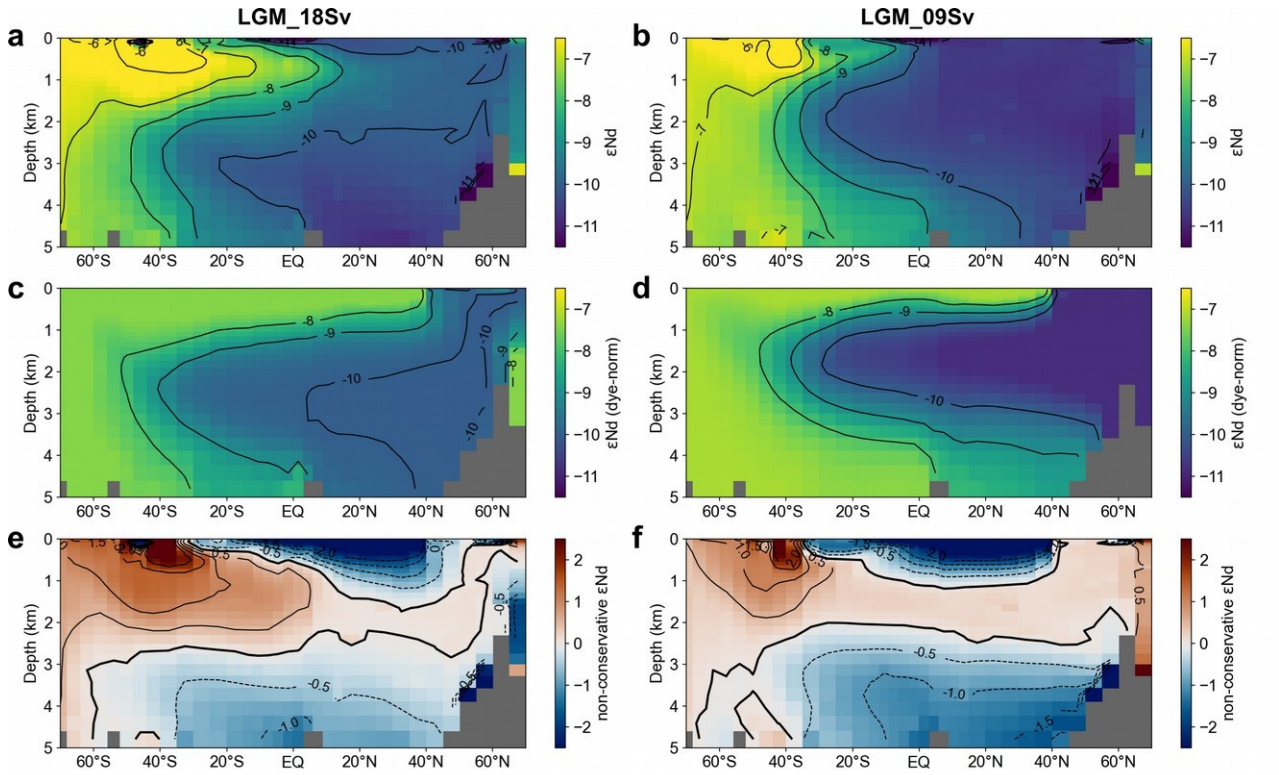

Figure S7: (a,b) Zonally averaged Atlantic εNd distribution. **(c,d)** Fully conservative part of the zonally averaged Atlantic εNd distribution of panel a. For this decomposition the true water mass distribution of the dye tracer (Figure 6) was renormalized by the Nd end-member characteristics at 50°N – 2.6 km water depth and 60°S – 3.1 km water depth. See supplementary text S2 for details on the calculation. **(e,f)** Difference between panels a and b, representing the non-conservative fraction of the εNd distribution. Left: LGM_18Sv and right: LGM_09Sv.

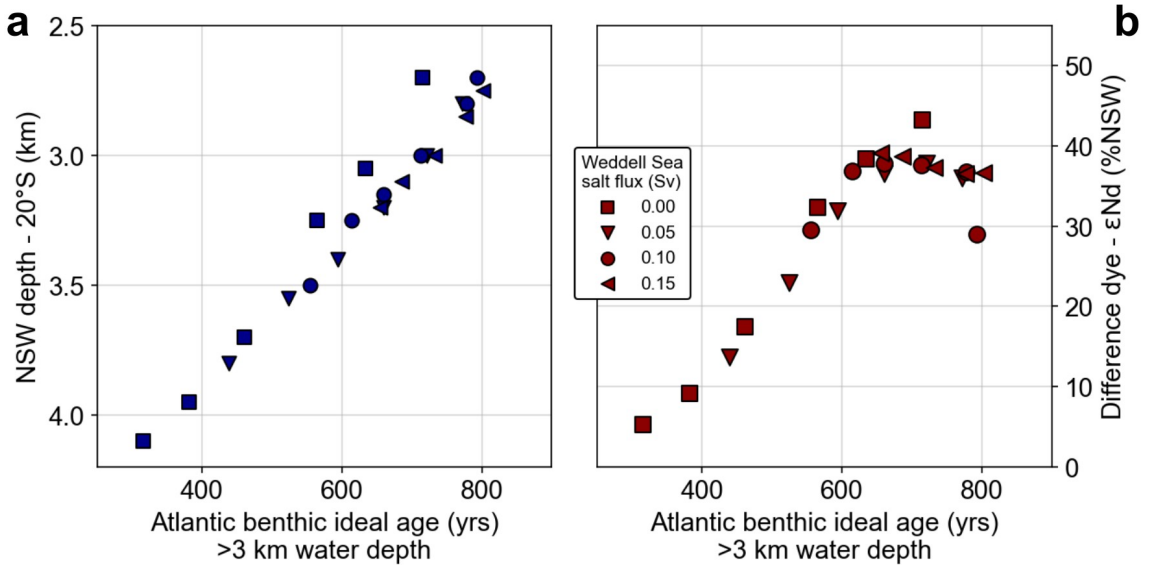

Figure S8 The mean Atlantic benthic (i.e., bottommost grid cell) ideal age below water depths of 3 km versus **(a)** the NSW depth at 20°S and **(b)** the overestimation of %NSW by εNd at 20°N. The benthic ideal age can be considered as a proxy for the benthic residence time and thus the impact of the benthic Nd flux on the bottom water isotopic signatures.

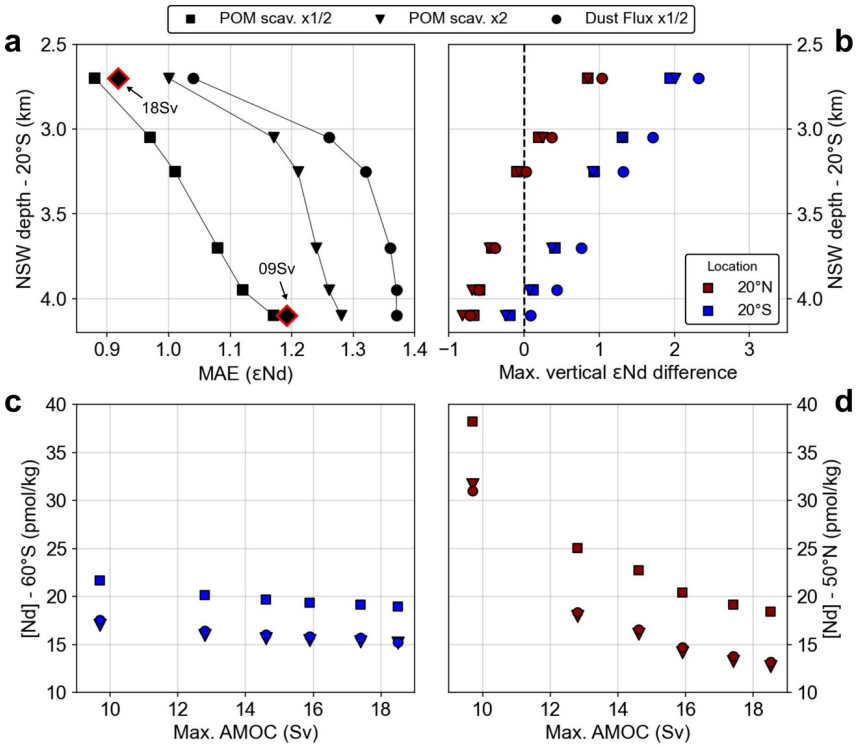

Figure S9: Sensitivity tests for LGM simulations with no Weddell Sea salt flux forcing (cf. Figure 4) for which the particle scavenging affinity to POM was halved (squares) or doubled (triangles), or the global dust flux halved (circles). **(a)** MAE versus the South Atlantic NSW depth for these simulations. **(b)** Maximum vertical εNd difference between NSW and SSW. **(c,d)** Nd concentrations at 60°S and 50°N both zonally averaged at 3 km water depth.

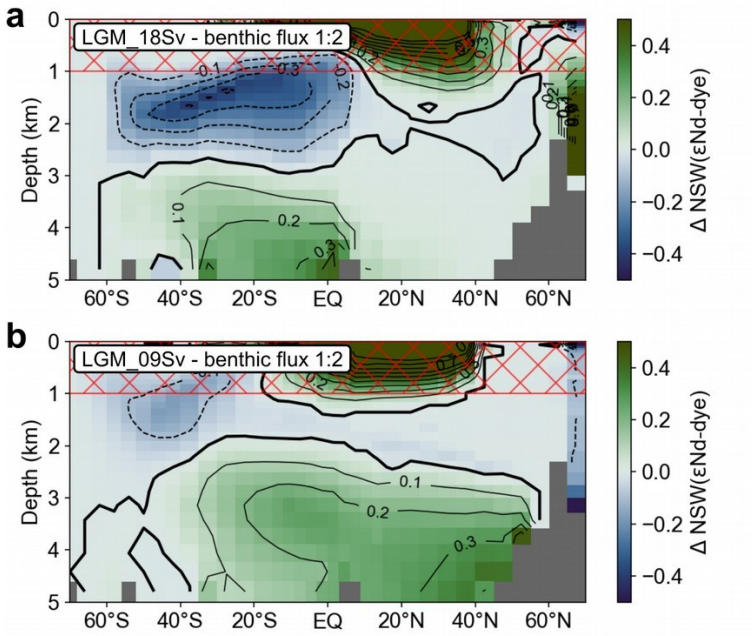

Figure S10: (a) LGM_18Sv and **(b)** LGM_09Sv sensitivity tests for which the parameterization of the calculation of the benthic flux isotopic composition was changed to weight the detrital and bottom water signatures from a 2:1 ratio in the standard setup (cf. section 2.1) to a 1:2 ratio. For this parameterization it is thus assumed that 67% of the benthic Nd flux is derived from authigenic phases that redissolve in the porewater and only 33% of the benthic Nd flux is contributed by Nd from the dissolution of detrital phases. In this case the deep Atlantic overprinting is about 10% less (in absolute terms) than in the standard setup (cf. Figure 7).

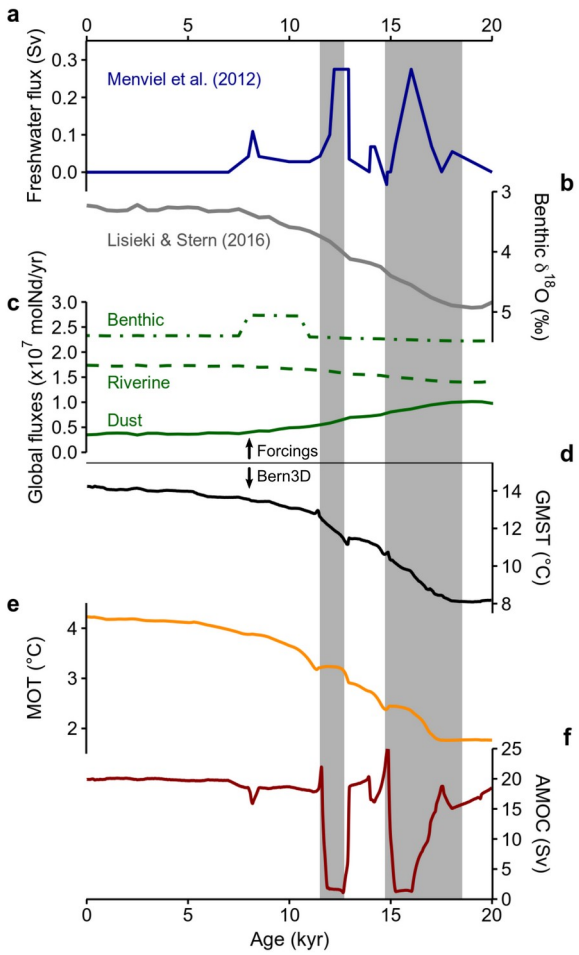

Figure S11: Timeseries of **(a)** freshwater (Menviel et al., 2012) and **(b)** benthic $\delta^{18}O$ (Lisiecki and Stern, 2016) forcings. Temporal evolution of **(c)** the Global Mean Surface Temperature (GMST), **(d)** the Mean Ocean Temperature (MOT), and **(e)** the AMOC strength of the transient simulations starting from LGM_18Sv.

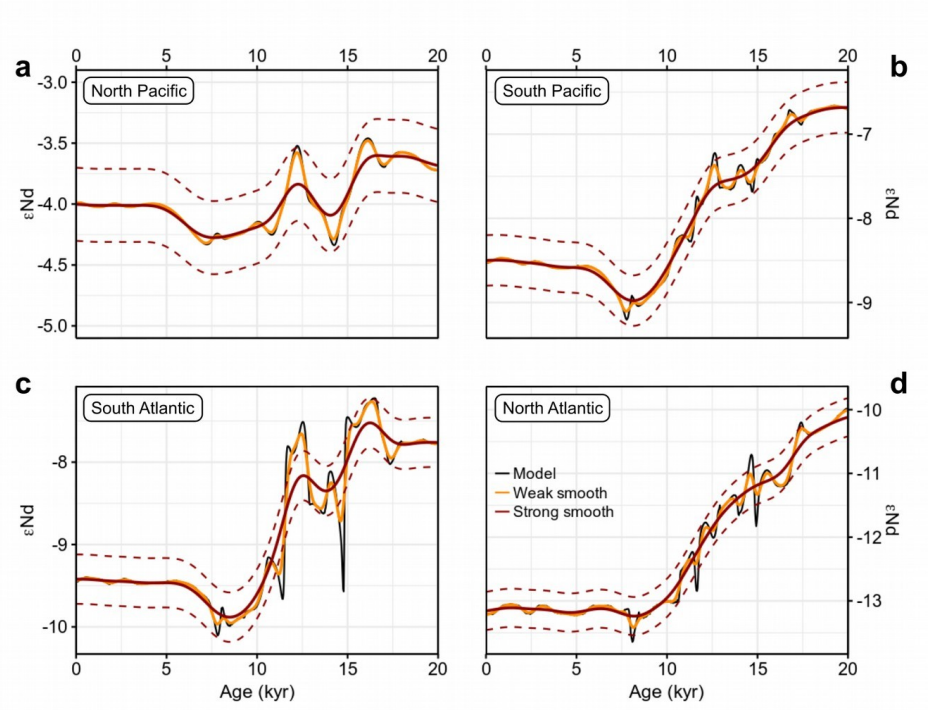

Figure S12: Simulated effect of bioturbation with gaussian kernel smoothing on the εNd timeseries shown in Figure 11e. The model output (black) is compared to weak (orange) and strong (red) smoothing. Dashed red lines indicate a typical analytical uncertainty of 0.3 ε-units relative to the strongly smoothed curve.

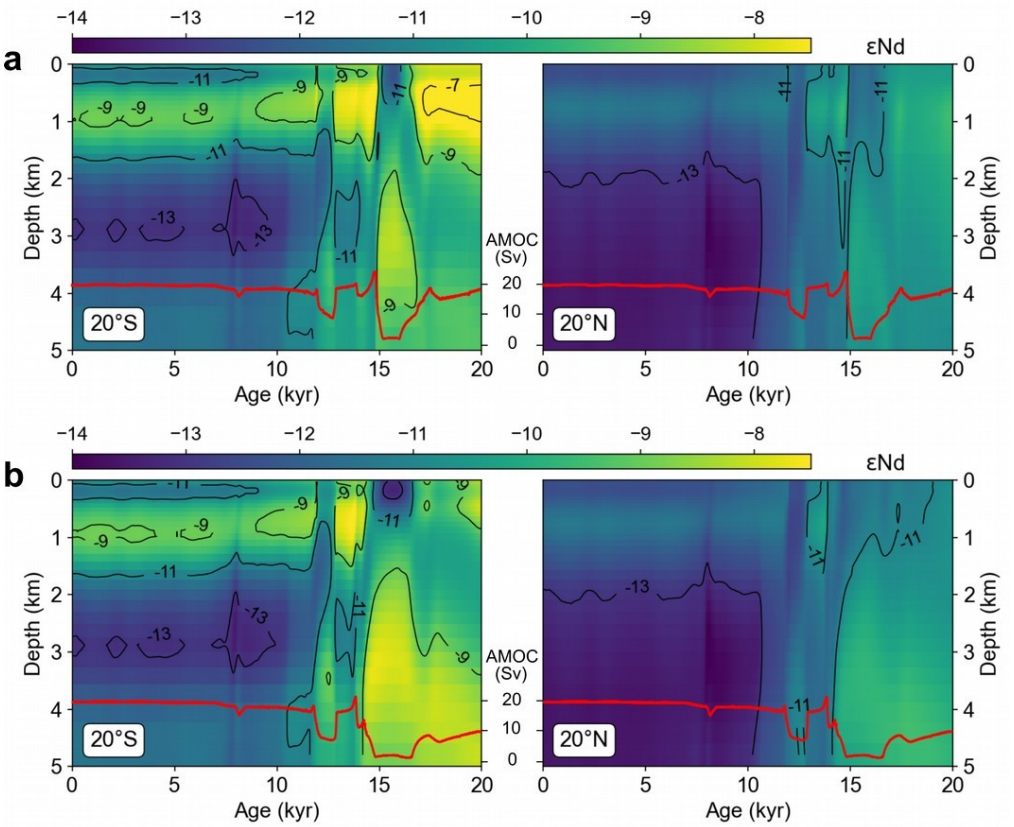

Figure S13: Same as Figure 12 but with a freshwater hosing flux half the size during the Younger Dryas that consequently leads to a smaller response in the AMOC strength.

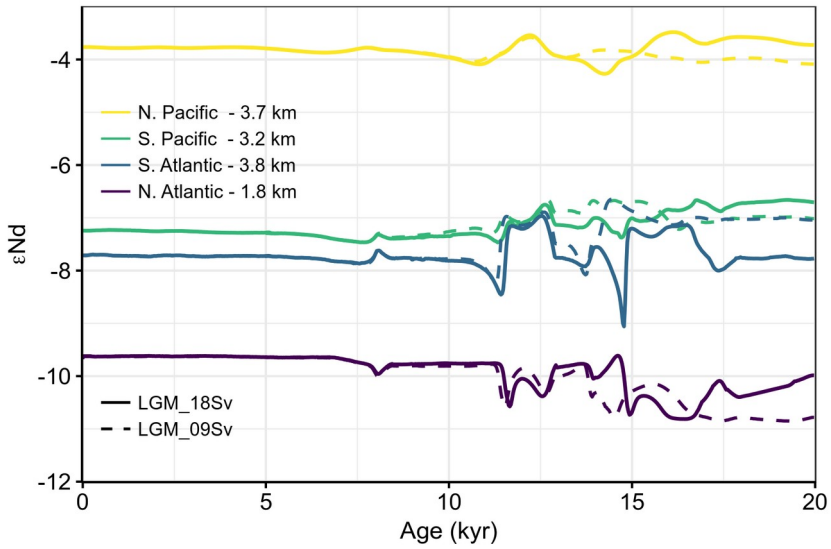

Figure S14: Simulated εNd timeseries at the locations of the exemplary sites depicted in Figure 10e for transient runs with constant LGM Nd forcing, but all other climatic, oceanic, and biogeochemical changes as in Figure 11.

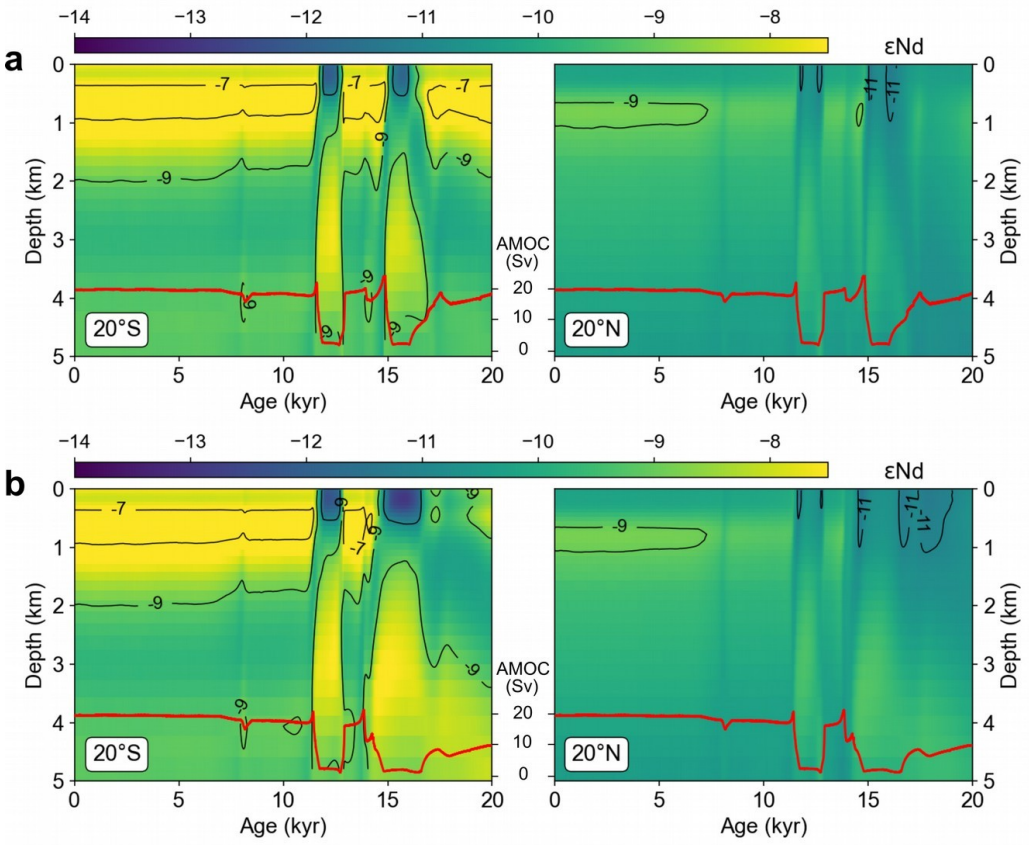

Figure S15: Same as Figure 12 but for constant LGM Nd forcing.

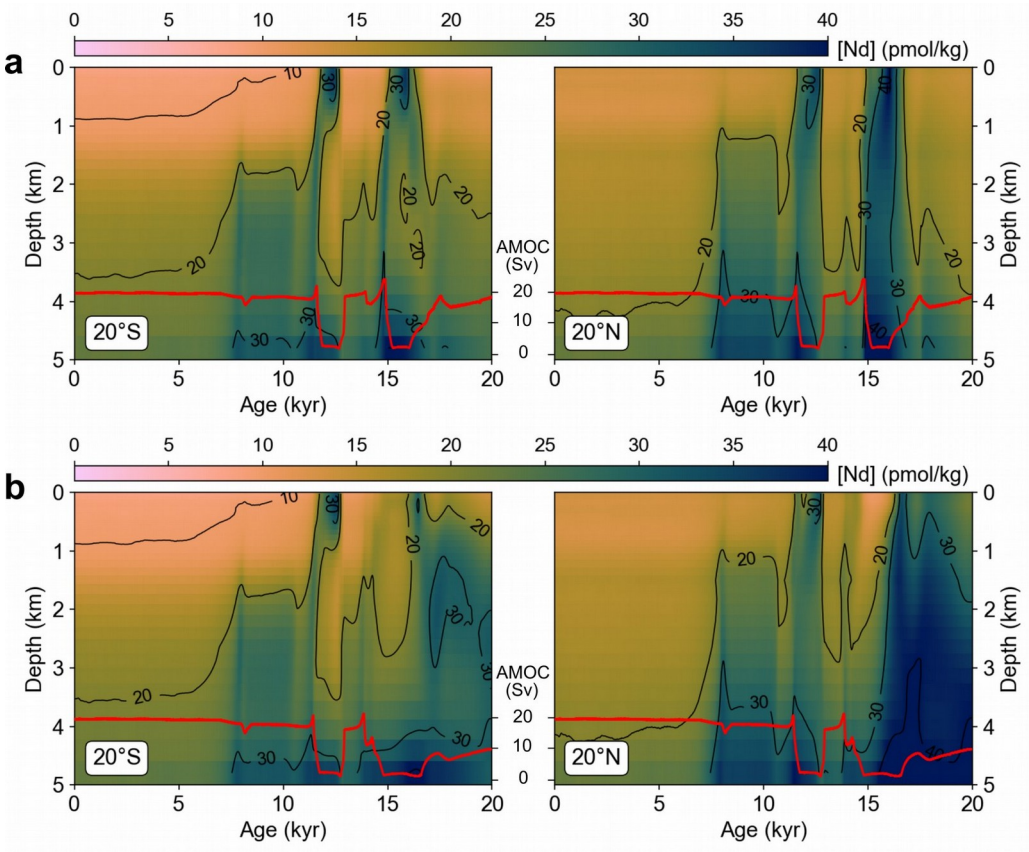

Figure S16: Hovmoller plots of the Nd concentration simulations **(a)** LGM_18Sv and **(b)** LGM_09Sv zonally averaged over the Atlantic at 20°S (left) and 20°N (right). Red lines mark the evolution of the AMOC strength.

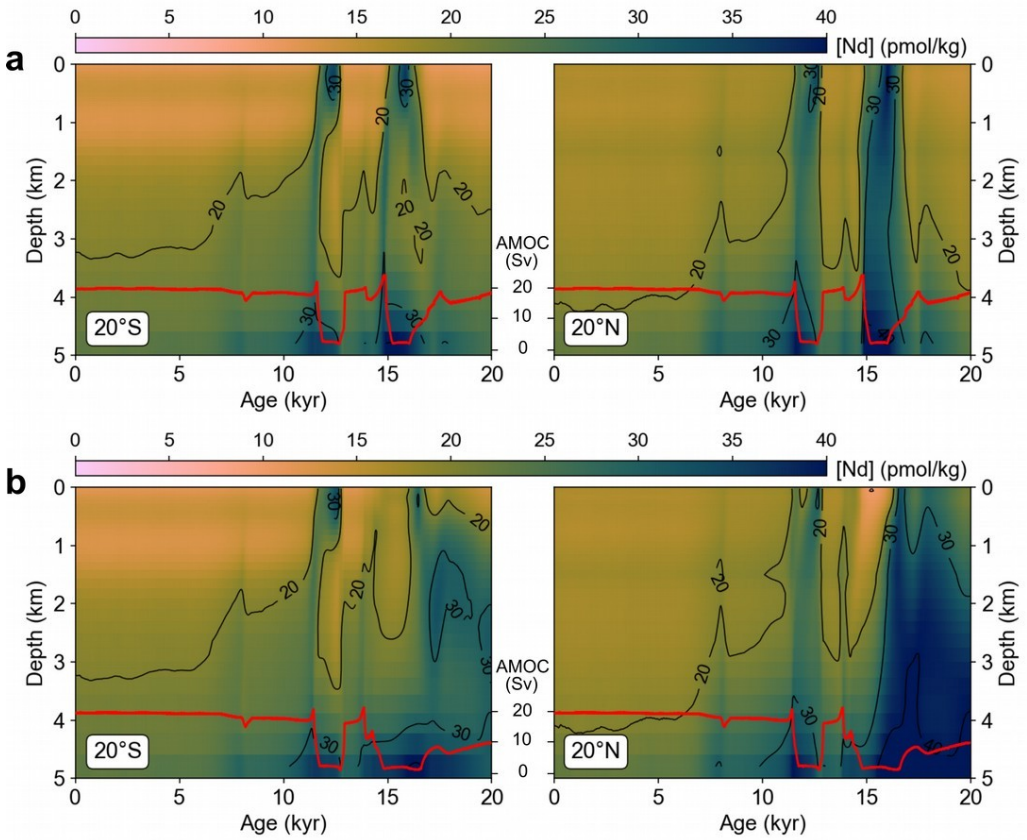

Figure S17: Same as Figure S16 but for constant LGM Nd forcing.

References

Berger, A.L., 1978. Long-Term Variations of Daily Insolation and Quaternary Climatic Changes. J. Atmos. Sci. 35, 2362–2367. https://doi.org/10.1175/1520-0469(1978)035<2362:LTVODI>2.0.CO;2

Hopcroft, P.O., Valdes, P.J., Woodward, S., Joshi, M.M., 2015. Last glacial maximum radiative forcing from mineral dust aerosols in an Earth system model. J. Geophys. Res. 120, 8186–8205. https://doi.org/10.1002/2015JD023742

Köhler, P., Nehrbass-Ahles, C., Schmitt, J., Stocker, T.F., Fischer, H., 2017. A 156 kyr smoothed history of the atmospheric greenhouse gases CO_2, CH_4, and N_2O and their radiative forcing. Earth Syst. Sci. Data 9, 363–387. https://doi.org/10.5194/essd-9-363-2017

Lisiecki, L.E., Stern, J. V, 2016. Regional and global benthic $\delta^{18}O$ stacks for the last Glacial Cycle. Paleoceanography 31, 1368–1394. https://doi.org/10.1002/2016PA003002

Mahowald, N.M., Muhs, D.R., Levis, S., Rasch, P.J., Yoshioka, M., Zender, C.S., Luo, C., 2006. Change in atmospheric mineral aerosols in response to climate: Last glacial period, preindustrial, modern, and doubled carbon dioxide climates. J. Geophys. Res. Atmos. 111, D10202. https://doi.org/10.1029/2005JD006653

Martin, J.H., Knauer, G.A., Karl, D.M., Broenkow, W.W., 1987. VERTEX: carbon cycling in the northeast Pacific. Deep Sea Res. Part A, Oceanogr. Res. Pap. 34, 267–285. https://doi.org/10.1016/0198-0149(87)90086-0

Menviel, L., Joos, F., Ritz, S.P., 2012. Simulating atmospheric CO_2, ^{13}C and the marine carbon cycle during the Last Glacial-Interglacial cycle: Possible role for a deepening of the mean

remineralization depth and an increase in the oceanic nutrient inventory. Quat. Sci. Rev. 56, 46–68. https://doi.org/10.1016/j.quascirev.2012.09.012

Peltier, W.R., 1994. Ice Age Paleotopography. Science. 265 (5169), 195–201. https://doi.org/10.1126/science.265.5169.195

Pico, T., Mitrovica, J.X., Mix, A.C., 2020. Sea level fingerprinting of the Bering Strait flooding history detects the source of the Younger Dryas climate event. Sci. Adv. 6. https://doi.org/10.1126/sciadv.aay2935

Pöppelmeier, F., Scheen, J., Blaser, P., Lippold, J., Gutjahr, M., Stocker, T.F., 2020. Influence of elevated Nd fluxes on the northern Nd isotope end member of the Atlantic during the early Holocene. Paleoceanogr. Paleoclimatology 35, e2020PA003973. https://doi.org/10.1029/2020pa003973

Pöppelmeier, F., Scheen, J., Jeltsch-Thömmes, A., Stocker, T.F., 2021. Simulated stability of the Atlantic Meridional Overturning Circulation during the Last Glacial Maximum. Clim. Past 17, 615–632. https://doi.org/10.5194/cp-17-615-2021

Robinson, S., Ivanovic, R., Flierdt, T. Van De, Blanchet, L., Tachikawa, K., Martin, E.E., Falco, C.P.C., Williams, T., Gregoire, L., Plancherel, Y., Jeandel, C., Arsouze, T., 2021. Global continental and marine detrital εNd: An updated compilation for use in understanding marine Nd cycling. Chem. Geol. 567, 120119. https://doi.org/10.1016/j.chemgeo.2021.120119

Tachikawa, K., Athias, V., Jeandel, C., 2003. Neodymium budget in the modern ocean and paleo-oceanographic implications. J. Geophys. Res. 108, 3254. https://doi.org/10.1029/1999JC000285